AIAA Propulsion and Energy Forum
August 9-11, 2021, VIRTUAL EVENT
AIAA Propulsion and Energy 2021 Forum

10.2514/6.2021-3382

Check for updates

Optimization of an ECR Thruster using Single, Two Frequency, and Pulsed Waveforms

Benjamin N. Wachs* and Benjamin A. Jorns †
University of Michigan, Ann Arbor, MI, 94109

The performance of an ECR magnetic nozzle thruster is optimized using custom waveforms. Single frequency, two-frequency, and pulsed microwave inputs are investigated. Performance is measured for single and two-frequency heating using a sub-millinewton thrust stand. A total of 245 points are tested using an automated global optimization algorithm. Holding forward power and flow rate constant at 30 W and 1 sccm xenon, it is found that thruster efficiency varies from 4.2% to 9.9% using single frequency heating over the range of 1050-2500 MHz. Adding a second frequency is not found to significantly affect performance. The results are discussed in the context of thruster physics and future thruster design.

I. Introduction

Magnetic nozzle thrusters are one of several technologies under development to address the need for low-power, high specific impulse, in-space propulsion. These thrusters operate by heating and accelerating a plasma through an expanding DC magnetic field [1]. The thermal energy, which is predominantly stored in the plasma electrons, is converted to ion kinetic energy as the plasma expands through the magnetic field. Typically these devices use radiofrequency or microwave power to heat the plasma, which enables electrode-free operation. This thruster architecture has several attributes that make it well suited for small satellite propulsion. For example, the lack of electrodes allows for reactive propellants and potentially low erosion operation. Similarly, the design requires only a single power supply.

Recent developments using Electron Cyclotron Resonance (ECR) as a heating source in magnetic nozzle thrusters have yielded promising results in comparison to previous designs. Thrust stand measurements have shown thrust efficiencies above 10% with specific impulses over 1000 seconds at 30 watts [2]. This is several times higher than the published data for low-power helicon and inductively coupled plasma designs [3]. With that said, while the performance of ECR thrusters is promising, the levels are still not competitive for mission application. In order to fully demonstrate the potential for this technology, there is a pressing need to identify technical paths to more rapidly advance its maturity. To this end, previous parametric experiments have shown that small changes to thruster geometry can have large effects on overall performance, indicating potential for further performance optimization [4].

An alternative methodology for improving ECR performance is to manipulate the power conditioning of the microwaves input to the thruster. For example, multiple waves with different frequencies are mixed before injected into the thruster or the amplitudes are modulated in a pulsed way. The hypothesis underlying the wave-mixing approach is that altering the power conditioning may change the location and size of the ECR resonance zone. Using pulsed power, on the other hand, allows the thruster to break free of normal limitations that stem from 0D power balance. This enables plasma properties, i.e. high electron temperatures. Both types of power conditioning have been implemented successfully on ECR ion sources used for heavy ion production to date [5]. However, they have not yet been explored for thrusters.

One of the major challenges with adopting this approach to optimization is the dimensionality of the problem. Without complete models of the underlying physics, optimization requires a gradient-free approach. With only two free parameters, exploring the design space can require tens or hundreds of sample points. Thus the need is apparent for tools that can more efficiently test each design point. The goal of this work is to explore strategies for optimizing the performance of a low power ECR thruster with traditional single frequency operation, two-frequency heating, and pulsed operation. We use a surrogate-based optimization algorithm to guide the exploration of parameter space in each case.

This paper is organized in the following way. We first motivate our study in Sec. II by introducing a global model of the thruster that we use to determine key optimization parameters. In Sec. III we describe the experimental setup including the thruster, vacuum facilities, and diagnostics used. Section IV details the optimization procedure and

*PhD. Candidate, Department of Aerospace Engineering, AIAA Student Member.
†Assistant Professor, Department of Aerospace Engineering, AIAA Associate Fellow

Copyright © 2021 by the American Institute of Aeronautics and Astronautics, Inc. All rights reserved.

Downloaded by UNIV OF MICHIGAN on August 31, 2021 | http://arc.aiaa.org | DOI: 10.2514/6.2021-3382

Downloaded by UNIV OF MICHIGAN on August 31, 2021 | http://arc.aiaa.org | DOI: 10.2514/6.2021-3382

algorithms employed during the experiment. In Sec. V, we present the results of our optimization experiments, and in Sec. VI we discuss the implications of our findings including physical insights and suggestions for future work.

II. Approaches to power conditioning

We motivate our optimization studies by examining the underlying performance drivers of magnetic nozzle thruster efficiency. Physics-based modelling of magnetic nozzle thrusters is an active area of research [6–9]. The devices involve complex processes including wave coupling, cross-field diffusion, and plasma detachment from magnetic field lines. Previous models have spanned full electromagnetic solvers [9] to quasi-1D [7] to fully 0D models [10]. Quasi-1D and 0D models tend to be independent of the plasma heating method and can therefore be used to model ECR as well as helicon or inductively coupled plasma discharges.

In this section, we use a 0D model to examine performance trends of a magnetic nozzle thruster. Our models are based on those given in Refs. [10] and [11]. We employ a control volume analysis to solve the coupled ion particle, neutral particle, and electron energy balances. The ion particle balance is as follows:

$$\mathcal{V}\frac{\mathrm{d}n_\mathrm{e}}{\mathrm{d}t} = K_\mathrm{iz}n_\mathrm{e}n_\mathrm{g}\mathcal{V} - n_\mathrm{e}u_\mathrm{B}\left(h_R\left(2\pi Rl\right) + h_{BW}\left(\pi R^2\right) + h_T\left(\pi R^2\right)\right), \tag{1}$$

where n_e and n_g are the plasma and neutral densities, respectively. The first term on the right represents the ion generation rate where K_{iz} is the ionization rate constant based on a Maxwellian electron population and $\mathcal{V}$ is the effective volume of the source. The second term on the right represents the ion loss rate where $u_\mathrm{B} = (qT_e/m_i)^{1/2}$ is the Bohm speed, R, l are the plasma source's radius and length respectively. The h factors, h_R, h_{BW}, and h_T are the sheath edge-to-center density ratios for the radial walls, back wall, and exit plane, respectively, with h_R encapsulating the plasma's radial confinement in the source.

The neutral particle balance used in our model is

$$\mathcal{V}\frac{\mathrm{d}n_\mathrm{g}}{\mathrm{d}t} = \frac{\dot{m}}{m_i} + n_\mathrm{e}u_B\left(h_R\left(2\pi Rl\right) + h_{BW}\left(\pi R^2\right)\right) - n_\mathrm{g}\left(\pi R^2\right)\frac{u_\mathrm{therm}}{4} - K_\mathrm{iz}n_\mathrm{e}n_\mathrm{g}\mathcal{V}. \tag{2}$$

Here, the first term on the right accounts for the propellant fed to the thruster with $\dot{m}$ the propellant mass flow rate and m_i is the ion mass. The second term on the right is the neutral particles gained from ion recombination on the radial and back walls of the thruster. The third term is the neutral particles lost to diffusion out of the thruster's exit plane with $u_\mathrm{therm} = \left(8k_BT_g/\pi m_i\right)^{(1/2)}$ being the average thermal speed. Here, we have assumed uniform neutral density and free molecular flow, likely an underestimate of the true, spatially varying, density. The last term is the neutrals lost to ionization collisions.

The power balance is as follows:

$$P_\mathrm{abs}(t) = \frac{\mathrm{d}}{\mathrm{d}t}\left(\frac{3}{2}en_\mathrm{e}\mathrm{T_e}\right)\mathcal{V} + P_\mathrm{c} + P_\mathrm{i} + P_\mathrm{e} + P_\mathrm{e,T}, \tag{3}$$

where P_abs is the power absorbed by the plasma electrons. Here, P_c, P_i, P_e, $P_\mathrm{e,T}$ are the components of power lost to electron-neutral collisions, ion kinetic energy at the sheath edge, electron energy at the radial and back wall sheath edges, and electron energy lost at the thruster exit plane, respectively. We define these powers as:

$$P_\mathrm{c} = en_\mathrm{e}n_\mathrm{g}\mathcal{V}_{eff}\left(K_\mathrm{iz}\mathcal{E}_\mathrm{iz} + K_\mathrm{ex}\mathcal{E}_\mathrm{el}\right) \tag{4}$$

$$P_\mathrm{i} = e\frac{1}{2}\mathrm{T_e}n_\mathrm{e}u_\mathrm{B}\left(h_R\left(2\pi Rl\right) + h_{BW}\left(\pi R^2\right) + h_T\left(\pi R^2\right)\right) \tag{5}$$

$$P_\mathrm{e} = e\left(V_\mathrm{s} + 2T_\mathrm{e}\right)n_\mathrm{e}u_\mathrm{B}\left(h_R\left(2\pi Rl\right) + h_{BW}\left(\pi R^2\right)\right) \tag{6}$$

$$P_\mathrm{e,T} = e\left(2T_\mathrm{e} + \frac{1}{2}M_{det}^2T_\mathrm{e}\right)n_\mathrm{e}u_\mathrm{B}\left(h_T\pi R^2\right), \tag{7}$$

where $\mathcal{E}_\mathrm{iz}$ and $\mathcal{E}_\mathrm{ex}$ are the ionization and average excitation energies for xenon and V_S is the sheath potential, $V_S = \frac{T_e}{2}\ln\frac{m_i}{2\pi m_e}$. M_{det} is the ion Mach number (u_i/u_B) at the nozzle location at which ions detach from magnetic field lines. The detachment speed and location are complex functions of electron heat flux and cross field diffusion physics that are active areas of research. As such, M_{det} is left as a free parameter in our model.

The model used here assumes fully uniform plasma and neutral densities, Maxwellian electrons, a single ion detachment point, and does not account for multiply charged ions, gas heating, or multi-step ionization. As such, we use it for studying performance trends and not absolute thrust predictions.

A. Steady state parameter sweep

In this section, we use our model to simulate the effects of decreasing wall losses, increasing ion Mach number, and changing the effective ionization volume. For all simulations, we set total input power to 30 W and flow rate to 1 sccm Xe. We show the time resolved results of a typical simulation in Fig. 1. For this case we set $h_R = 0.5$, $M_{det} = 2$, and $\mathcal{V}$ is equal to the thruster's volume. Fig. 1a shows the applied power vs. time and Fig. 1 shows the resulting electron temperature and plasma density. We use the quasi-steady state results at the end of the simulation to calculate predicted thrust and efficiency.

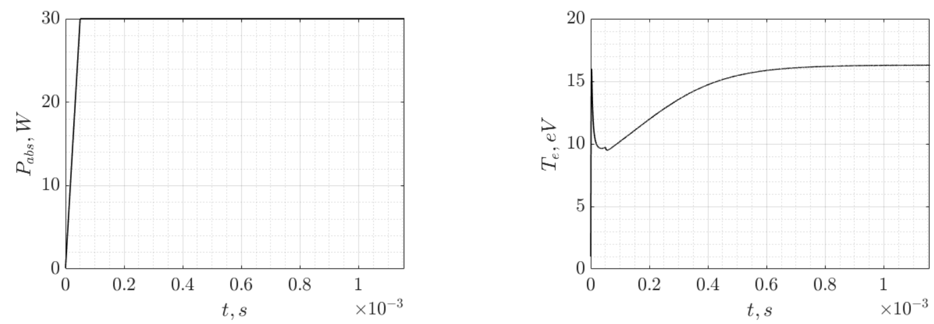

(a) **(b)**

Fig. 1 Time resolved global model showing (a) absorbed power (b) electron temperature & electron density.

Using this tool, we sweep h_R, M_{det}, and $\mathcal{V}_{eff}$, an effective volume for ionization. The results of this study are shown in Fig. 2. For the nonswept parameters, we use the a default of $h_R = 0.5$, $M_{det} = 2$, and $\mathcal{V}_{eff}/\mathcal{V} = 1$.

Downloaded by UNIV OF MICHIGAN on August 31, 2021 | http://arc.aiaa.org | DOI: 10.2514/6.2021-3382

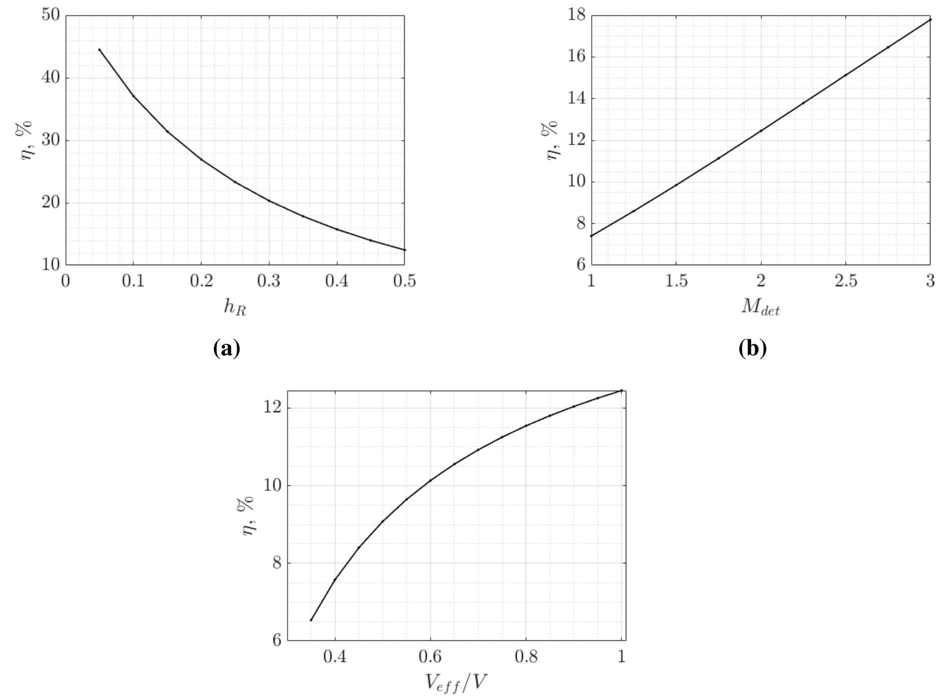

(a) **(b)**

(c)

Fig. 2 Parameter sweeps showing simulated efficiency vs. (a) radial confinement parameter, h_R, (b) detachment Mach number, M_{det}, and (c) effective volume for ionization, V_{eff}.

From this study, it is evident that the most important driver of thruster efficiency, for the power and flow rate simulated, is wall losses, with detachment Mach number and effective ionization volume playing smaller, but significant roles.

B. Single & two-frequency optimization

Based on the above parameter sweep, our goals in producing a higher performance thruster are to decrease plasma diffusion to the thruster walls (decrease h_R), increase ion detachment Mach number, and increase the volume over which plasma is generated. By changing the size and location of the ECR resonance zone, we aim modify these properties, though the underlying physics is not fully understood.

C. Pulsed optimization

In this section, we use our global model to simulate pulsed operation of the thruster. As in the previous section, we simulate thruster performance with an average input power of 30 W and a flow rate of 1 sccm xenon. We show a typical time resolved result in Fig. 3. Here, the pulse period is 100μS and the duty cycle is 50%.

Downloaded by UNIV OF MICHIGAN on August 31, 2021 | http://arc.aiaa.org | DOI: 10.2514/6.2021-3382

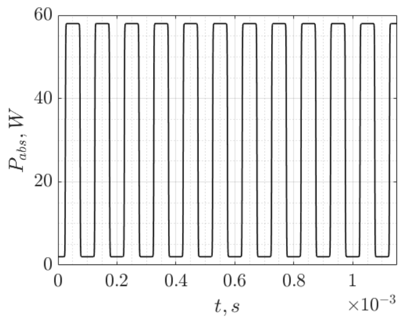

(a)

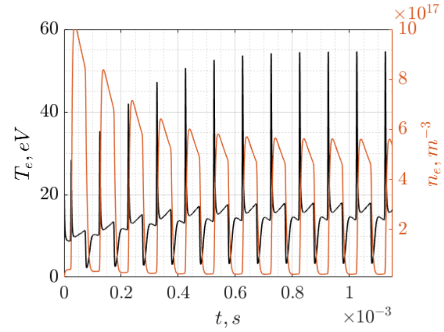

(b)

Fig. 3 Pulsed power time resolved global model showing (a) absorbed power (b) electron temperature & electron density.

Using this tool, we simulate the predicted performance from 20 to 100% duty cycle. The results are shown in Fig. 4.

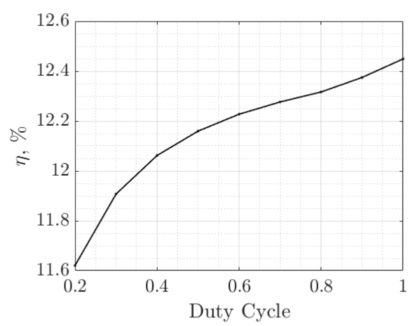

Fig. 4

The simulations predict that the highest efficiency is reached at CW operation. The lower performance predicted during pulsed operation is caused by a lower predicted mass utilization efficiency. These results indicate that single and two-frequency heating may yield better performance than pulsed power operation.

III. Experimental Setup

The experimental setup is comprised of six main components: the thruster, microwave generator, microwave power sensors, thrust stand, LabVIEW control, and the optimization algorithm. Each test point is selected by the optimization algorithm, which feeds the test parameters to the LabVIEW program. The program then sets and monitors the thruster test point. Once reaching a stable condition, the thrust stand measures thrust, which is then input to the optimization algorithm. The process continues until an optimum point is found or the the experiment is manually terminated.

A. Thruster

We performed our investigation with a coaxial type ECR thruster (Fig. 5), similar to those developed by ONERA [12]. It has a central conductor to excite a transverse electromagnetic (TEM) wave in the plasma discharge region, which in turn creates resonant heating within the thruster where $\omega_{ECR} = q_e B/m_e$, where q_e is the elemtary charge, B is the magnetic field strength, and m_e is the electron mass. The thruster body is made from a 6061 aluminum alloy, and the center conductor is graphite. The magnetic field is generated using a set of samarium cobalt magnets with a maximum operating temperature of 350 C. The simulated center-line magnetic field strength is shown in Fig. 6. Given the magnetic field strength, we expect that the ECR condition to be satisfied for frequencies ranging from 2979 MHz (exit plane) to 1080 MHz (back plane). Throughout the experiments, we used xenon propellant at a flow rate of 1 SCCM. The power input to the thruster was held constant at 30 W.

Downloaded by UNIV OF MICHIGAN on August 31, 2021 | http://arc.aiaa.org | DOI: 10.2514/6.2021-3382

Downloaded by UNIV OF MICHIGAN on August 31, 2021 | http://arc.aiaa.org | DOI: 10.2514/6.2021-3382

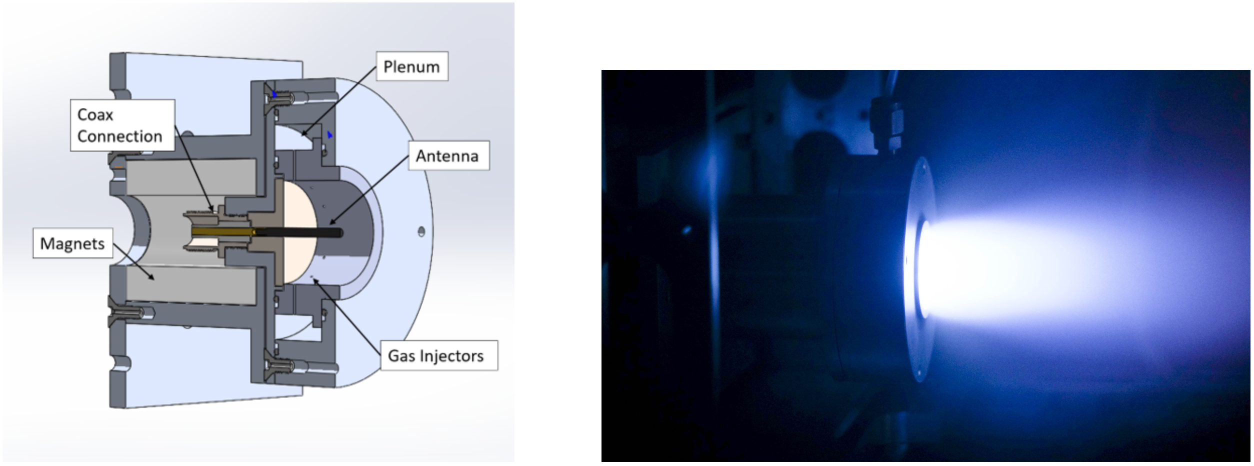

(a) **(b)**

Fig. 5 (a) Schematic of ECR thruster CAD (b) image of ECR thruster firing at 30 W and 1 sccm xenon.

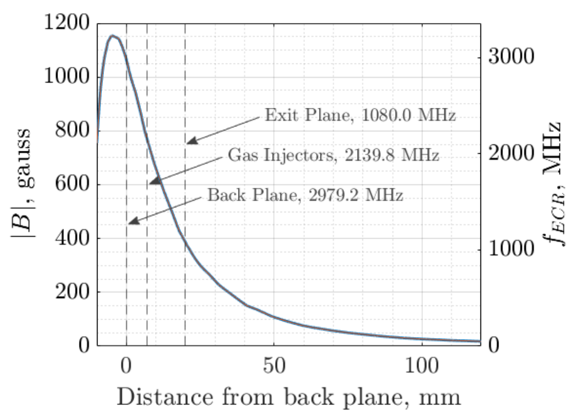

Fig. 6 Simulated magnetic field strength along thruster centerline. The corresponding cyclotron frequencies are indicated at key locations.

B. Microwave generation and diagnostics

We show a schematic diagram of the microwave equipment used in the experiments in Fig. 7. The setup uses a dual-output computer-controlled microwave signal source (WindFreak Synth HD Pro) to generate the single, two-frequency, and pulsed waveforms in the experiments. These signals are combined (in the case of two frequency heating) using a 3 dB combiner and fed to a solid-state power amplifier (Comtech PST ARD88258-50). The amplifier increases the input signal to 30 W. The operational bandwidth of the amplifier spans from 800-2500 MHz, making it the limiting component in selecting output frequencies. We tapped the output of the amplifier with a 20 dB directional coupler (Mini-Circuits ZGBDC20-372HP+) and connected these ports to two thermocouple-based power sensors (Keysight N8482H) to measure forward and reverse power to the thruster.

Downloaded by UNIV OF MICHIGAN on August 31, 2021 | http://arc.aiaa.org | DOI: 10.2514/6.2021-3382

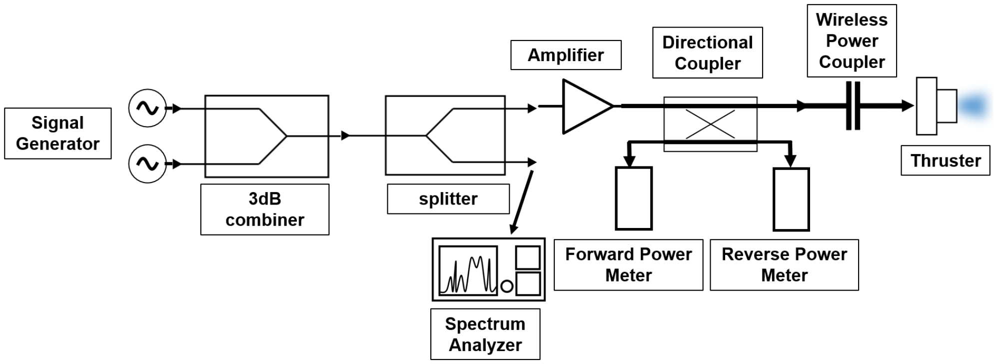

Fig. 7 Schematic of microwave equipment used in the optimization experiments

C. Thrust Stand

We used a custom designed counter-weighted hanging pendulum thrust stand to measure thrust output, similar to that used in [13]. The thrust stand is shown inside the vacuum facility in Fig. 8. The design uses a fiber-optic displacement sensor (Philtec D63) to measure changes in the pendulum arm position. The displacement sensor is read by a DAQ at 200 samples/s and averaged over 5 seconds to generate thrust readings. By shifting the position of the counterweight, the sensitivity of the thrust stand can be adjusted. The expected thrust output for our experiment lies in the range of 0.1 - 0.8 mN.

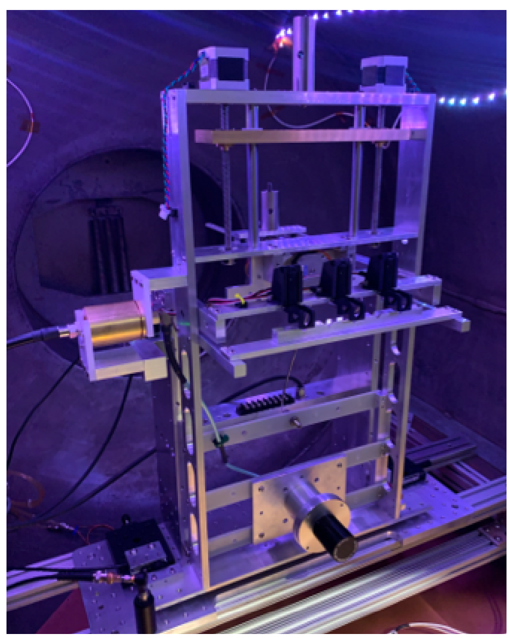

Fig. 8 Hanging pendulum thrust stand used in experiments

We calibrate the thruster by dropping known masses on a fixed moment arm. The calibration force can be calculated as $F_{cal} = \frac{l_{cal}}{l_T} g m_{cal}$, where l_{cal} is the calibration mass moment arm, l_T is the center of thrust moment arm, g is earth's gravitational acceleration, and m_{cal} is the calibration mass. For the thrust stand used in these experiments, $\frac{l_{cal}}{l_T} = 1/3$.

We show the output of a typical thrust measurement in Fig. 9. Here, thrust is measured by taking the difference between the test point and a low-power default point. We use this procedure to avoid having to restart the plasma for each thrust measurement. Using a linear fit, we can detrend the thrust data to eliminate errors caused by thermal drift, which produces the result shown in Fig. 9b.

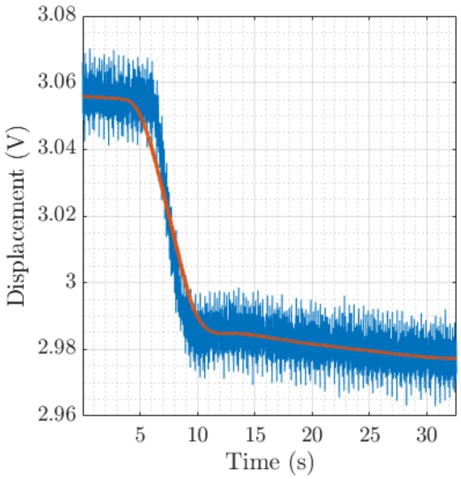

(a)

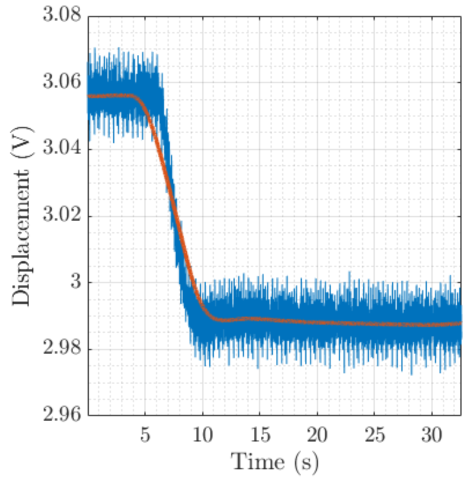

(b)

Fig. 9 (a) Typical relative thrust measurement, (b) thrust measurement with linear detrending applied

In order to verify that the thruster was not giving erroneous data caused by microwave interference, we attached a dummy load to the thruster and recorded the data as microwave power (30 W) was turned on and off. The results are shown in Fig. 10. While there is substantial thermal displacement during the test, the drift remains roughly linear over the time period (15 seconds) required for measuring thrust. Furthermore, there are no abrupt changes to the drift when power to the dummy load is turned off.

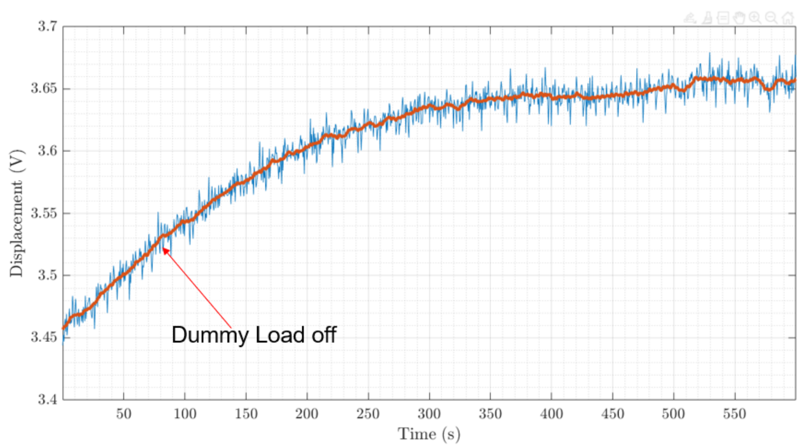

Fig. 10 Displacement vs. time for the dummy load test

1. Wireless Power Coupler

In order to avoid measurement errors caused by thermally expanding RF cables, we employed a wireless power coupler to transmit microwave power to the thrust stand (Fig. 11). This coupler has a coaxial geometry with rotational symmetry that allowed the coupler to rotate about the pendulum axis during measurements. A 1mm gap between coupler halves allowed for frictionless movement, greatly increasing the thrust stand's sensitivity while eliminating a major source of error.

Downloaded by UNIV OF MICHIGAN on August 31, 2021 | http://arc.aiaa.org | DOI: 10.2514/6.2021-3382

Downloaded by UNIV OF MICHIGAN on August 31, 2021 | http://arc.aiaa.org | DOI: 10.2514/6.2021-3382

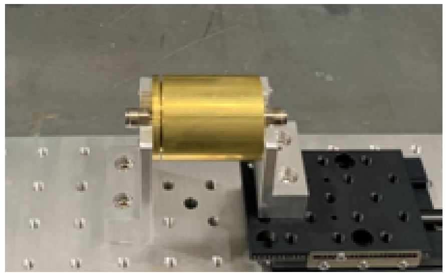

Fig. 11 Wireless power coupler used on thrust stand

D. Vacuum Facility

The experiments in this paper were conducted in the Junior Test Facility at the University of Michigan's Plasmadynamics and Electric Propulsion Laboratory, shown in Fig. 12. The chamber measures 1×3 meters and is equipped with a turbomolecular and cryogenic pumps that have a combined pumping speed of 32,000 l/s for xenon. We measure chamber pressure with a Stabil Series 370 Ion Gauge. The base pressure throughout the experiment was measured to be below 10^{-7} Torr-N_2 throughout the experiment.

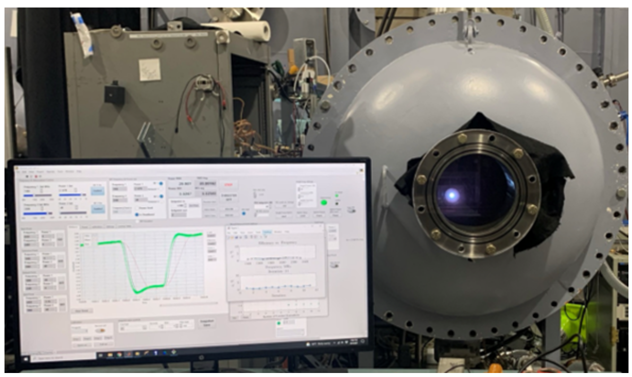

Fig. 12 Junior Test Facility with Optimization Experiment Running

IV. Methods

A. Optimization procedure

The overarching goal of the experiment is to increase the thruster's efficiency, η, defined as $\eta = T^2/(2\dot{m}P)$, where T is the measured thrust, $\dot{m}$ is the propellant mass flow rate, and P is the power input to the thruster. For the purposes of our experiment, we hold the total input power and mass flow rate constant at 30W, 1 SCCM-Xe, though future experiments could allow these parameters to vary. We quantified the power to the thruster, P, using the forward power measurement. Although reflected power can be, in theory, delivered to the plasma through the use of a matching network, we do not make this assumption in calculating our efficiency.

We begin the experiments by measuring thrust at a default low-power operating point of 7W, 2400 MHz. During the optimization process, we measure only the difference in displacement, δ, between the test point and a default low-power operating point. By measuring changes in thrust, as opposed to taking absolute thrust measurements, we were able to keep the plasma lit throughout the experiments. We averaged the displacement and microwave power readings over 5 seconds when taking each thrust point. We transitioned between test points using an automated sequence during which the thruster was kept in a powered on state to avoid time consuming restarts. Each modulation scheme requires a unique transition procedure to keep the thruster stable while switching test points. Each new trial point transition and measurement required approximately one minute to complete.

Downloaded by UNIV OF MICHIGAN on August 31, 2021 | http://arc.aiaa.org | DOI: 10.2514/6.2021-3382

1. Single Frequency Optimization

The single frequency optimization experiment seeks to find the frequency, f, that maximizes thruster efficiency. For this experiment, f ranges from 1050 MHz to 2500 MHz. The lower frequency bound is dictated by the thruster's stability while the upper frequency bound is imposed by the amplifier's bandwidth. Initial tests showed that at frequencies below 1050 MHz, the thruster could not sustain the 30W, 1 sccm discharge for more than a few seconds. It is worth noting that the magnetic field strength at the exit plane of the thruster corresponds to a resonant frequency of 1080 MHz, indicating that the ECR resonance zone should be located within the thruster for stable operation.

The single frequency experiment used the following procedure: The thruster is warmed up at 30 W, 1 sccm-xe for approximately one hour. The thruster is then transitioned to the default low-power point and the optimizer is initiated. The optimizer selects a test point and sends a command to the signal generator to switch frequencies. A software-controlled PID loop is then called to stabilize the thruster at 30 W. Once the thruster reaches 30 W +/- 0.4 W for 5 seconds, the PID loop is turned off. The thruster is kept at its current state for 10 seconds and then transitioned to the default low-power set-point to measure thrust. The single frequency optimization experiment uses 20 randomized points to seed the optimizer.

2. Two Frequency Optimization

The two-frequency optimization experiment seeks to find the frequency combination, (f_1, f_2), that maximizes thruster efficiency. Here, the total power, 30 W, is split equally between f_1 and f_2. For this experiment, f_1 ranges from 1050 MHz to 2500 Mhz while f_2 ranges from 1000 to 2540 MHz. The minimum frequency gap between f_1 and f_2 is set to 50 MHz. The experiment used the following procedure: The thruster is warmed up at 30 W, 1 sccm-xe for approximately one hour. The thruster is then transitioned to the default low-power point and the optimizer is initiated. The optimizer selects a test point consisting of frequencies (f_1, f_2). The thruster is then transitioned to run at frequency f_1. The PID loop is then enabled, bringing the thruster to 15 W. Once the thruster is stable at 15 W, the PID controller is turned off and the second frequency, f_2, is enabled. A PID loop controlling the power applied at f_2 is then enabled. The PID loop then brings the total power to 30 W. When the thruster reaches 30 W +/- 0.4 W for 5 seconds, the PID loop is turned off the thruster is held at its current operating point for 10 seconds at which point thrust is measured.

B. Optimization Algorithm

We used an off-the-shelf surrogate based global optimization algorithm to select each new test point [14]. The algorithm builds a surrogate model of the system based on radial basis functions. It selected each test point using a combination of expected improvement and uncertainty in its model. The algorithm was seeded with several randomly selected test points to initialize the test. The single frequency experiments used 20 randomly sampled points while the two-frequency and pulsed experiments used 50. The algorithm will reset to random samples when it predicts little improvement with each new sample point.

V. Results

In this section, we detail our findings for each of the modulation schemes used in the optimization experiments. We first start with the single frequency results, and then describe the two-frequency results.

A. Single Frequency Results

We ran the single frequency optimization experiment through a total of 34 iterations with 20 randomly selected seed points.With only one variable, this experiment could have used predetermined test points without sacrificing too much time. However, using the global optimization algorithm allowed this experiment to serve as a proof of concept for future experiments with larger design spaces. The total amount of time it took to run all 34 points was 45 minutes. The results are shown in Fig. 13. Fig. 13a shows the efficiency as a function of frequency. Fig.13b shows the frequency as a function of actual iteration number. This underscores how the optimizer employs a combination of randomization and guided search to narrow on a region of optimal efficiency. Ultimately, by varying the frequency from 1050 to 2500 MHz, the resultant efficiencies ranged from under 4.2% to 9.9%, indicating that thruster performance is strongly dependent on input frequency. The highest measured efficiency was (9.9%) was measured at 2498 MHz, near the back wall of the thruster.

Downloaded by UNIV OF MICHIGAN on August 31, 2021 | http://arc.aiaa.org | DOI: 10.2514/6.2021-3382

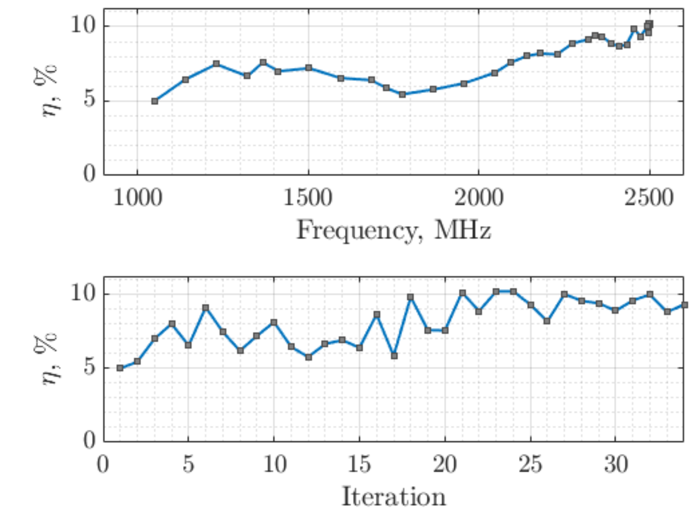

(a)

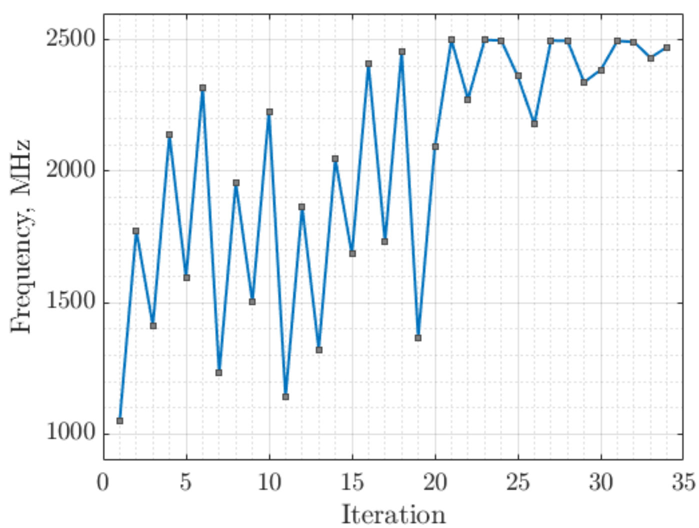

(b)

Fig. 13 Results of the single frequency optimization experiment. (a) efficiency vs frequency & iteration number, (b) frequencies selected by the optimizer

B. Two Frequency Results

Using two frequencies opens the allowable design space to a nearly infinite combination of inputs and thus greatly increases the number of trials needed to find an optimum. The experiment is seeded with 50 randomly selected points. We show results of a 211 point two-frequency optimization experiment in Fig. 14. Fig. 14a shows the efficiency as a function of frequency. Fig.14b shows the efficiency as a function of actual iteration number.

The resultant efficiencies range from 3.2% to 10.3%, again indicating the thruster's performance is strongly dependent on the input waveform. The highest efficiency was measured at f_1 = 1202 MHz, f_2 = 2540 MHz. It is worth noting that the optimum point includes a high frequency component, similar to the single frequency results.The preliminary data show that two-frequency heating does not significantly improve performance over the best single frequency trials. We note, however, that the parameter space has yet to be fully explored.

Downloaded by UNIV OF MICHIGAN on August 31, 2021 | http://arc.aiaa.org | DOI: 10.2514/6.2021-3382

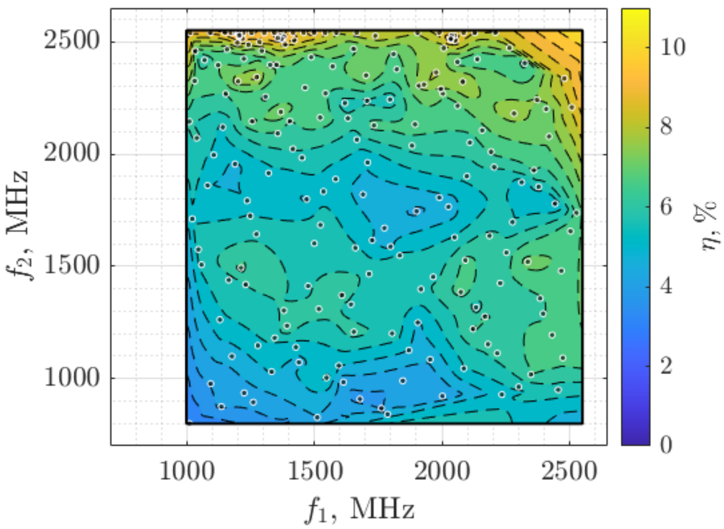

(a)

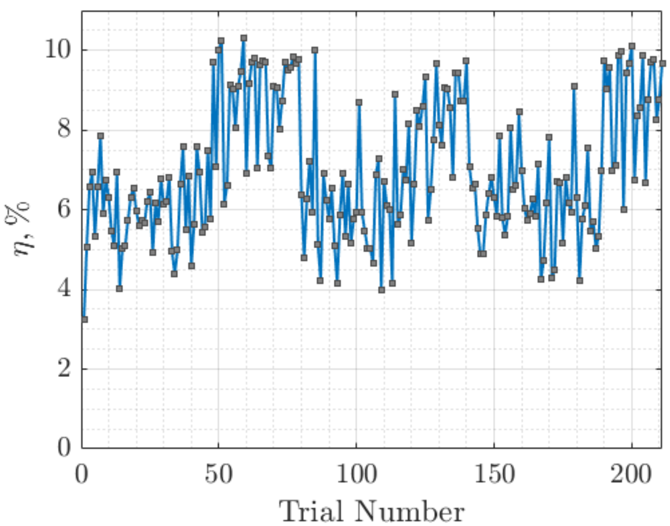

(b)

Fig. 14 Results of the two-frequency optimization experiment. (a) Efficiency vs. f_1, f_2. (b) Efficiency vs. trial number.

VI. Discussion

The results show that thruster performance is strongly dependent upon the input waveform. In the case of two-frequency heating, efficiencies improved almost 3× from 3.2% to 10.3% comparing the maximum and minimum performance test points.

Looking at the single frequency results (Fig. 13), we observe that the maximum efficiency occurs around the highest frequency tested, 2500 MHz, with another peak occurring around 2340 MHz. These frequencies correspond to resonance zones near the back wall of the thruster, upstream of the propellant injection (Fig. 6). This trend could indicate that more efficient heating occurs closer to the source of the microwave energy, where the wave does not need to penetrate the plasma as far to reach the ECR condition. However, this theory would indicate a monotonic decrease in performance as frequency is lowered, a trend not observed in the data. Alternatively, the higher efficiency frequencies could correspond to plasma densities favorable to ECR absorption. If this were the case, we would expect different

Downloaded by UNIV OF MICHIGAN on August 31, 2021 | http://arc.aiaa.org | DOI: 10.2514/6.2021-3382

propellant flow rates to produce different efficiency versus frequency responses. Finally, more complex microwave coupling effects, such as resonances within the thruster, could lead to high efficiency frequencies.

The two-frequency experiment demonstrated that adding a second resonance zone does not significantly affect the thruster's performance. Examining the data, we can observe that by taking the maximum of f_1 and f_2 (f_{max}) for each trial, the performance follows a similar trend to the single frequency results. This analysis is shown in Fig. 15. These data indicate that the maximum frequency largely dictates thruster performance. This result indicates that the location of the first resonance zone has more of an effect on the overall plasma properties than downstream resonance zones.

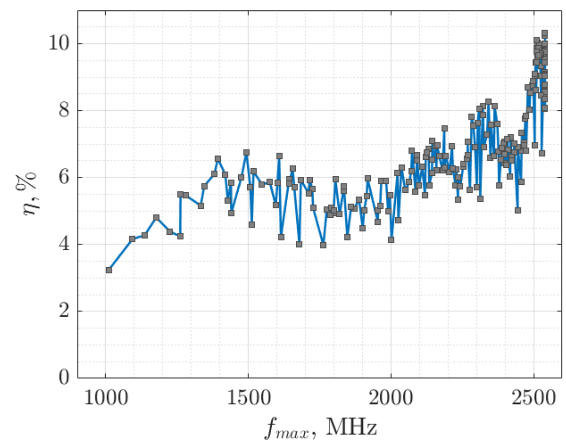

Fig. 15 Efficiency vs maximum frequency for the two frequency optimization experiment

VII. Conclusion

In this paper, we have shown that ECR thruster performance is highly sensitive to the input waveform, with efficiencies ranging from 3.2% to 10.3%. Our experiments demonstrated that by changing the input frequency of a single-frequency ECR thruster, we could more than double thrust efficiency. However, our experiments indicated that two-frequency heating does not add significant efficiency gains compared to the optimized single frequency results.

To our knowledge, this work demonstrates the first real time optimization of a thruster of this class. More broadly, the algorithm and framework we have developed here have demonstrated a new and potentially highly enabling methodology for more rapidly exploring and optimizing new technologies

VIII. Acknowledgments

This work was supported by NASA Space Technology Research Fellowship grant 80NSSC17K0157. Thank you to Eric Viges for getting the vacuum systems running, and to the fellow members of the Plasmadynamics and Electric Propulsion Laboratory for their support and many insightful conversations.

References

[1] Bathgate, S. N., Bilek, M. M. M., and Mckenzie, D. R., "Electrodeless plasma thrusters for spacecraft: a review," *Plasma Science and Technology*, Vol. 19, No. 8, 2017, p. 083001. https://doi.org/10.1088/2058-6272/aa71fe, URL http://stacks.iop.org/1009-0630/19/i=8/a=083001?key=crossref.4d1f338161907e428a54432c8bc6ab12.

[2] Vialis, T., Jarrige, J., Aanesland, A., and Packan, D., "Direct Thrust Measurement of an Electron Cyclotron Resonance Plasma Thruster," *Journal of Propulsion and Power*, Vol. 34, No. 5, 2018, pp. 1323–1333. https://doi.org/10.2514/1.B37036, URL https://doi.org/10.2514/1.B37036.

[3] Siddiqui, U., and Cretel, C., "Updated Performance Measurements and Analysis of the Phase Four RF Thruster," *2018 Joint Propulsion Conference*, American Institute of Aeronautics and Astronautics, Cincinnati, Ohio, 2018. https://doi.org/10.2514/6.2018-4817, URL https://arc.aiaa.org/doi/10.2514/6.2018-4817.

[4] Vialis, T., Jarrige, J., and Packan, D., "Geometry optimization and effect of gas propellant in an electron cyclotron resonance plasma thruster," Atlanta, GA, 2017.

[5] Rácz, R., Biri, S., Perduk, Z., Pálinkás, J., Mascali, D., Mazzaglia, M., Naselli, E., Torrisi, G., Castro, G., Cellona, L., Gammino, S., and Galata, A., "Effect of the two-close-frequency heating to the extracted ion beam and to the X-ray flux emitted by the ECR plasma," *Journal of Instrumentation*, Vol. 13, No. 12, 2018, pp. C12012–C12012. https://doi.org/10.1088/1748-0221/13/12/C12012, URL http://stacks.iop.org/1748-0221/13/i=12/a=C12012?key=crossref.71132ac235044e8b4cf7e12b75931680.

[6] Little, J. M., and Choueiri, E. Y., "Thrust and efficiency model for electron-driven magnetic nozzles," *Physics of Plasmas*, Vol. 20, No. 10, 2013, p. 103501. https://doi.org/10.1063/1.4824613, URL http://scitation.aip.org/content/aip/journal/pop/20/10/10.1063/1.4824613.

[7] Lafleur, T., "Helicon plasma thruster discharge model," *Physics of Plasmas*, Vol. 21, No. 4, 2014, p. 043507. https://doi.org/10.1063/1.4871727, URL http://aip.scitation.org/doi/10.1063/1.4871727.

[8] Ahedo, E., Correyero, S., Navarro-Cavallé, J., and Merino, M., "Macroscopic and parametric study of a kinetic plasma expansion in a paraxial magnetic nozzle," *Plasma Sources Science and Technology*, Vol. 29, No. 4, 2020, p. 045017. https://doi.org/10.1088/1361-6595/ab7855, URL https://iopscience.iop.org/article/10.1088/1361-6595/ab7855.

[9] Sánchez-Villar, , Zhou, J., Ahedo, E., and Merino, M., "Coupled plasma transport and electromagnetic wave simulation of an ECR thruster," *Plasma Sources Science and Technology*, Vol. 30, No. 4, 2021, p. 045005. https://doi.org/10.1088/1361-6595/abde20, URL https://iopscience.iop.org/article/10.1088/1361-6595/abde20.

[10] Lieberman, M. A., and Lichtenberg, A. J., *Principles of plasma discharges and materials processing*, 2nd ed., Wiley-Interscience, Hoboken, N.J, 2005. OCLC: ocm56752658.

[11] Lafleur, T., and Aanesland, A., "Ambipolar and non-ambipolar diffusion in an rf plasma source containing a magnetic filter," *Physics of Plasmas*, Vol. 21, No. 6, 2014, p. 063510. https://doi.org/10.1063/1.4885109, URL http://aip.scitation.org/doi/10.1063/1.4885109.

[12] Cannat, F., Lafleur, T., Jarrige, J., Chabert, P., Elias, P.-Q., and Packan, D., "Optimization of a coaxial electron cyclotron resonance plasma thruster with an analytical model," *Physics of Plasmas*, Vol. 22, No. 5, 2015, p. 053503. https://doi.org/10.1063/1.4920966, URL http://scitation.aip.org/content/aip/journal/pop/22/5/10.1063/1.4920966.

[13] Packan, D., Jarrige, J., Blanchard, C., Elias, P.-Q., Fallerini, L., and Noci, G., "Micronewton Balance Measurements at Onera and Application to the GAIA Mission," Washington, D.C., 2013. URL http://electricrocket.org/IEPC/f5i6xur1.pdf.

[14] Gutmann, H.-M., "A Radial Basis Function Method for Global Optimization," *Journal of Global Optimization*, Vol. 19, No. 3, 2001, pp. 201–227. https://doi.org/10.1023/A:1011255519438, URL https://doi.org/10.1023/A:1011255519438.

Downloaded by UNIV OF MICHIGAN on August 31, 2021 | http://arc.aiaa.org | DOI: 10.2514/6.2021-3382